Title
Vegetation responses to air dryness amplify future land surface warming

Journal
Nature Communications, 17(1)

ISSN
2041-1723

Authors
Green, Julia K
Keenan, Trevor F
Lian, Xu
et al.

Publication Date
2026-05-11

DOI
10.1038/s41467-026-73063-7

nature communications

Article

https://doi.org/10.1038/s41467-026-73063-7

Vegetation responses to air dryness amplify future land surface warming

Received: 3 December 2025

Accepted: 30 April 2026

Published online: 11 May 2026

Check for updates

Julia K. Green[1], Trevor F. Keenan[2,3], Xu Lian[4], David J. P. Moore[5] & Philippe Ciais[6]

Temperature exerts a first-order control on vegetation photosynthesis and transpiration. Yet most studies investigating temperature impacts on plants rely on near-surface air temperature, rather than canopy temperature—the temperature plants actually experience. Because canopy temperature directly regulates ecosystem function, it provides a more accurate measure of vegetation–climate interactions. Combining Earth System Model (ESM) simulations and satellite observations in a dual emergent constraint, here we show that canopy temperature is projected to increase substantially more than air temperature (~0.11-degrees more or a 16% increase in their difference) over the 21st century. The ESM ensemble median fails to capture these stronger increases in the majority of vegetated regions. We find that the largest projected increases in the difference between canopy and air temperature are predicted to occur in regions where elevating moisture stress—particularly rising vapor pressure deficit—increasingly constrains vegetation growth and transpiration. This implies that future warming will impose stronger constraints on plant function than currently estimated. Relying on air temperature alone will therefore lead to systematic underestimation of temperature effects on photosynthesis, vegetation growth, and the land carbon sink. Accurate representation of canopy temperature in ESMs is thus essential to improve projections of ecosystem responses and feedbacks to climate change.

Reducing CO_2 emissions to limit increases in global near-surface air temperature (Tair) is the focal point of climate policy and mitigation plans worldwide[1]. However, while Tair has important implications for human and environmental health, land surface temperature (LST), which reflects canopy temperature over vegetated surfaces, is more relevant to preserving plant biodiversity and maintaining ecological function[2,3]. While land- and near-surface air temperature tend to be highly correlated in space and time, their differences are driven by important physical and biological processes. These differences can reveal details about the canopy boundary layer and surface energy balance, including changes in wind speed, vegetation water stress, and vegetation distribution changes, all which govern evaporative conditions[4–6]. Thus, quantifying the difference between LST and Tair (ΔT), and determining how it will shift over the coming century can provide information to better understand ecosystem responses to environmental change, land-atmosphere feedbacks, and future changes to the land carbon sink. It can provide invaluable insight into how the Earth System will change with continued anthropogenic emissions and has the potential to reveal those regions and ecosystems most threatened in the future. Previous studies, however, have shown conflicting conclusions on current trends in LST related to cloud contamination, differing coverage, various sampling times, and instability

[1]Department of Environmental Science, University of Arizona, Tucson, AZ, USA. [2]Department of Environmental Science, Policy, and Management, University of California, Berkeley, CA, USA. [3]Earth and Environmental Sciences, Lawrence Berkeley National Laboratory, Berkeley, CA, USA. [4]Sino-French Institute for Earth System Science, College of Urban and Environmental Sciences, Peking University, Beijing, China. [5]School of Natural Resources and the Environment, University of Arizona, Tucson, AZ, USA. [6]Laboratoire des Sciences du Climat et de l'Environnement, Gif-sur-Yvette, France. e-mail: juliakgreen@arizona.edu

of satellite products[7,8], and how LST and its relationship with Tair will evolve in the future remains unclear.

While Tair is measured at globally distributed weather stations (albeit with certain regions better sampled than others), measurements of LST are derived from satellite retrievals and subject to multiple limitations. For example, thermal infrared (TIR) satellite observations are restricted to clear-sky conditions[9,10], which has been shown to cause overestimation of monthly LST by as much as 5.6 °C[11] because LST increases rapidly with incoming radiation during sunny episodes. This contrasts with many other cloud-free remote sensing data products, for example, the normalized difference vegetation index, which has less pronounced shifts between clear- and all-sky conditions. Meanwhile, LST retrieved from microwave satellite observations are hindered by coarse resolution, signal penetration into the soil, and lower accuracy[8]. These data limitations make it difficult to provide a high accuracy estimate of LST with long time series that can be used to benchmark Earth System Models (ESMs). Compared with Tair observations that show strong agreement among datasets (Supplementary Fig. 1), satellite LST products have been shown to be less stable[7], while the varying algorithms and wavelengths used for data retrieval contribute to large discrepancies between commonly used products such as MODIS 11[12], MODIS 21[13] and AIRS[14] (Supplementary Fig. 1). These LST data uncertainty issues have hampered our ability to accurately constrain LST, as well as the difference between LST and Tair on the regional or global scales.

Emergent constraints provide the opportunity to constrain all-sky (includes days with cloud coverage and precipitation) LST and ΔT in models despite these observational limitations. An emergent constraint is based on a heuristic relationship between an observable (all-sky Tair) and an unobservable variable (all-sky LST) represented across an ensemble of models[15,16], here ESMs from the Coupled Model Intercomparison Project Phase 6 (CMIP6)[17]. While individual ESMs may have biased values of LST and Tair, if the relationships between them are preserved across the model ensemble, then when examined collectively, the observed all-sky Tair can be used to constrain the ESM all-sky LST. Likewise, current and future ΔT values are empirically related across the ESM ensemble (Fig. 1a), providing a unique opportunity to use the difference between constrained all-sky LST in the present day and observation-based Tair, to constrain future estimates of ΔT.

In this study, using a suite of observation-based Tair datasets and the CMIP6 ESMs (Supplementary Table 1), we first constrained all-sky LST in the historical simulations (2000–2014) (Supplementary Fig. 2a, c, e, g) and used that to obtain an observation and model informed all-sky estimate of ΔT in the present day (ΔT_{obs}). To predict how ΔT will change in the future, we then used ΔT_{obs} in a second emergent constraint to constrain the difference between air and land surface temperature predicted by ESMs at the end of the 21st century, using a fossil-fueled development scenario, shared socioeconomic pathway 5-85 (SSP585; ΔT_{con_SSP585}) (Fig. 1 and Supplementary Fig. 2b, d, f, h). In addition to performing these analyses as global averages, the strong local relationships between historical ΔT_{obs} and future ΔT estimates across the ESM ensemble ($R^2 > 0.6$ in 96% of pixels; Supplementary Fig. 3), allowed for a pixel-by-pixel constraint of projected changes in ΔT and exploration of regional nuances (Fig. 1). The changes between ΔT_{con_SSP585} and ΔT_{obs} were further analyzed to understand the projected meteorological and ecological shifts that typically accompany ΔT changes. These analyses reveal climatic and ecosystem

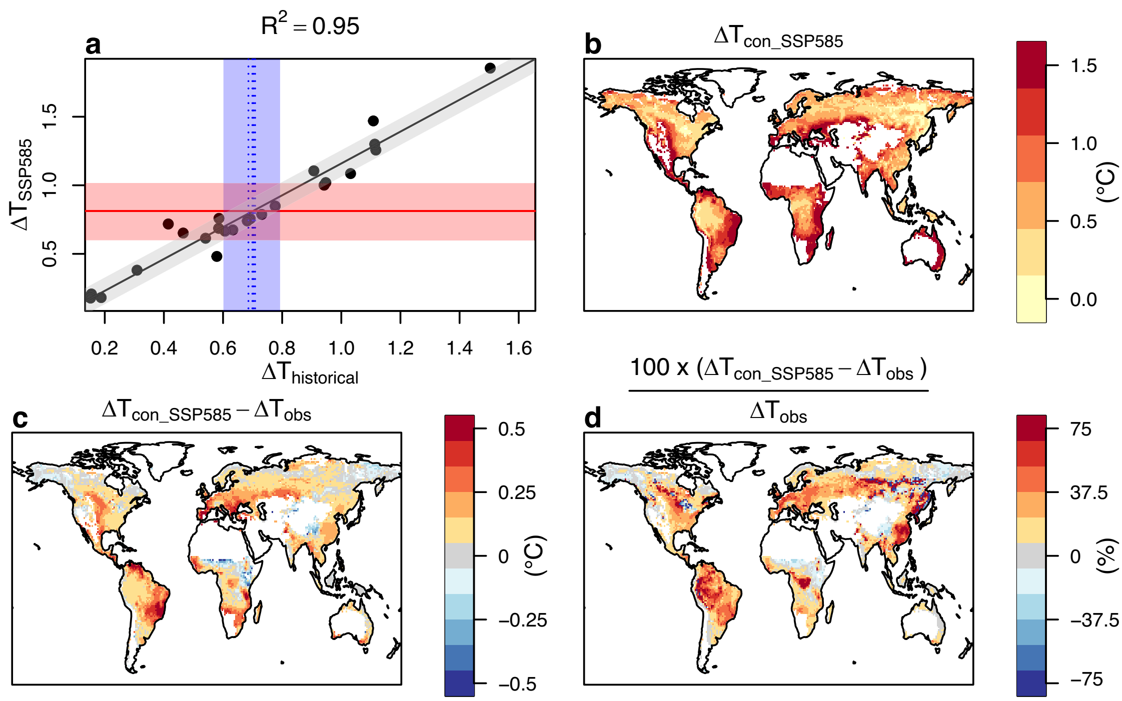

Fig. 1 | The difference between land surface and near-surface air temperature (ΔT) constrained by observations. a A constraint on ΔT across CMIP6 Earth System Models (ESMs) in the future SSP585 run for 2085-2099 (ΔT_{con_SSP585}) using the difference between constrained all-sky land surface temperature (LST) from the historical simulation and observational air temperature (Tair) (ΔT_{obs}) from four different Tair datasets, applied globally over vegetated regions. **b** The same constraint as subplot **a** applied pixel-by-pixel in vegetated regions globally. **c** The difference between ΔT_{con_SSP585} and ΔT_{obs}. **d** The percent change between ΔT_{con_SSP585} and ΔT_{obs}. In subplot **a**, each circle represents an individual ESM, the blue dashed vertical lines represent the ΔT_{obs} values from the four observation-based dataset combinations, the red horizontal line represents the constrained value (ΔT_{con_SSP585}) using the median observational Tair value for the constraint, and the solid diagonal line is the best linear fit of the data. Shaded regions represent uncertainty in the observation-based data (blue; standard deviation across the dataset combinations), regression (gray; standard error), and constrained values (red; the propagation of the standard deviation across the observation-based dataset combinations with the ESM linear regression standard error). All temperature units are in degrees Celsius. Vegetated regions are defined as regions with leaf area index greater than 1.

characteristics that could make a region more susceptible to future ΔT increases, and potentially more at risk for future vegetation shifts.

Results

Future amplification of the difference between LST and Tair (ΔT)

The dual constraint demonstrates that large, constrained increases in all-sky LST relative to Tair are projected from the present day towards the end of the 21st century (2085-2099; Fig. 1a, b). These could be caused by shifts in hydrometeorological conditions, such as precipitation patterns, winds, cloud coverage, or rising temperature and air dryness (e.g., vapor pressure deficit; VPD). They could also be caused by ecological changes, such as decreased stomatal conductance in response to increased plant physiological stress, CO_2 fertilization, or vegetation distribution changes. While all-sky LST averaged globally over vegetated land is currently ~0.70 °C ± 0.08 °C greater than Tair (uncertainty expressed as the standard deviation across the observation-based datasets), this value constrained increases to ~0.81 °C ± 0.20 °C in 2085–2099 (Fig. 1a) (uncertainty expressed as the propagation of the standard deviation across the observation-based datasets with the ESM linear regression standard error). Increases in ΔT are predicted to occur across ~81% of vegetated regions, with some regions predicted to experience increases as high as 0.5 °C by 2100.

The largest ΔT_{con_SSP585} occurs mainly in arid regions (defined as regions with an aridity index [AI = precipitation/potential evapotranspiration] <0.50), particularly those predicted to become dryer (Fig. 1b, Supplementary Figs. 4–6 and Supplementary Table 2). The largest future increases (ΔT_{con_SSP585} minus ΔT_{obs}) are expected to also occur in arid regions, although transitional subhumid regions (0.5 < AI < 0.65) predicted to become dryer also are predicted to have strong increases (Supplementary Fig. 6). These include grasslands in the Central US, and savannas in southeastern Brazil, Venezuela and Colombia (Fig. 1c, d). These regions are known to have strong land-atmospheric feedbacks, where drying conditions can self-amplify from reduced evapotranspiration, further drying the atmosphere locally and downwind[18–20], increasing ΔT. Other locations of large ΔT increases include croplands in the northern US, Canada and Europe, where croplands have been shows to have strong biophysical impacts on increasing LST[21], and the tropical forest region of Guyana, which certain studies have shown is at risk of transitioning to savanna[22].

Meanwhile, most humid regions with less extreme seasonal temperature fluctuations (e.g., equatorial regions) tend to have smaller constrained future ΔT increases in absolute terms (<0.2 °C), but these ΔT_{con_SSP585} values still correspond to ≈70% relative increases compared to the present day ΔT (e.g., the Congo rainforest, Amazon rainforest, and eastern Asia), with an average relative increase of 37% across evergreen broadleaf forests (Supplementary Fig. 7 and Supplementary Table 3). Tropical ecosystems, with minimal temperature seasonal variability and little exposure to large temperature oscillations, are less well-adapted to extreme heat, and thus these shifts can still have strong ecosystem impacts[23]. It should be noted that while evergreen broadleaf forests have an average ΔT increase of 0.12 °C which is among the highest of the PFTs (Supplementary Table 3), this value is largely dominated by the strong increases along the tropical rainforest edges and in Guyana.

Using random forest models (RFs) and interpretable machine learning diagnostics (Shapley values), we investigated environmental factors contributing to future ΔT changes. For predictors, we used data from the future and historical ESM simulations describing meteorological conditions, vegetation structure, and surface energy fluxes (Supplementary Fig. 8). For each predictor variable in each ESM, we took the average difference between the future and historical time periods and then took the median across the CMIP6 model ensemble (Methods). After removing predictors that were highly correlated and pruning the data to remove artefacts of spatial autocorrelation (Methods; Supplementary Fig. 9), we found that variations in future ESM ΔT changes across space could be largely explained ($R^2 = 0.75$ on out-of-bag data) by mean ESM ensemble projections of future changes in leaf area index (LAI), VPD and latent heat flux (Fig. 2), and that the importance of these three predictors was consistent across aridity gradients (Supplementary Fig. 10) and plant functional types (Supplementary Figs. 11–13). While VPD and soil moisture are often highly correlated, their future changes relative to the current day are not, because VPD is projected to increase globally while soil moisture projections are more varied[24]. It should be noted that Shapley values depict how a predictor influences a prediction to be above or below the mean value of the response variable (e.g., Shapley values less than 0 do not necessarily mean that the predictor is influencing ΔT to be less than 0).

Our results show that future LAI increases (partially from CO_2 fertilization[25]) have a reductive impact on future ΔT changes, because in the ESMs, higher LAI leads to higher transpiration rates and latent heat flux, cooling the land surface if soil moisture is not limiting. While future LAI increases may result in lower albedo, producing a warming effect from reduced net radiation, this is largely offset by the cooling effect of increased LAI on latent heat flux. This has been demonstrated previously in regards to land cover change[26]. This response is consistent across aridity gradients (Supplementary Fig. 10), and PFTs (Supplementary Fig. 11).

For meteorological shifts, regions with the largest future increases in ΔT relative to the historical period correspond to where ESM projections show the largest VPD increases and the greatest latent heat flux reductions (Fig. 2b–d). In these regions, surface moisture is likely low and limiting to evaporation, and thus future elevated VPD would increase ΔT through reduced evaporation (as moisture supply depletes) and latent heat flux as well as increased sensible heat flux (increasing ΔT). Simultaneously, changing meteorological conditions would impact ΔT through vegetation feedbacks. Lower water availability and higher VPD would cause vegetation water stress, resulting in reduced stomatal conductance, transpiration, and latent heat flux (Fig. 2c, d). As more available energy at the land surface would be consequently converted to sensible heat flux, the vegetation would contribute to ΔT increases as vegetated canopies would warm more with an attenuated cooling effect of transpiration. This could further become a feedback loop in ESMs, because increased ΔT combined with moisture stress could reduce rates of transpiration and LAI through reduced photosynthesis, further contributing to the persistence of elevated ΔT. This is consistent across aridity gradients (Supplementary Fig. 10) and PFTs (Supplementary Fig. 12), including in very wet evergreen broadleaf forests (tropical rainforests), which are thought to be already operating near their photosynthetic temperature optima (Topt)[23]. These results agree with previous findings showing that high VPD can increase ΔT in tropical rainforest regions, even where soil moisture might not be depleted[5].

It is possible that regions that are most at risk for future loss of resilience and exacerbation of vegetation stress, are those regions predicted to have the largest relative future increases in ΔT and are located in transitional regimes bordering other ecosystem types. This is because transitional areas can be 'bistable', making them more susceptible to state changes than other areas, as they share similar climatic conditions to bordering ecosystems, and might only need small environmental perturbations to transition[27]. These areas include the Central US expanding into southern Canada, a region located between humid environments to the east and dry environments to the west, and southern Europe, located between humid regions to the north and dry regions to the south. It also includes the edges of tropical forest regions (dominated by evergreen broadleaf vegetation), frequently bordered by savannas. It is also possible that acclimation to warmer temperatures may occur[28] and Topt may increase, a process that ESMs may not represent well, and thus it is especially important to

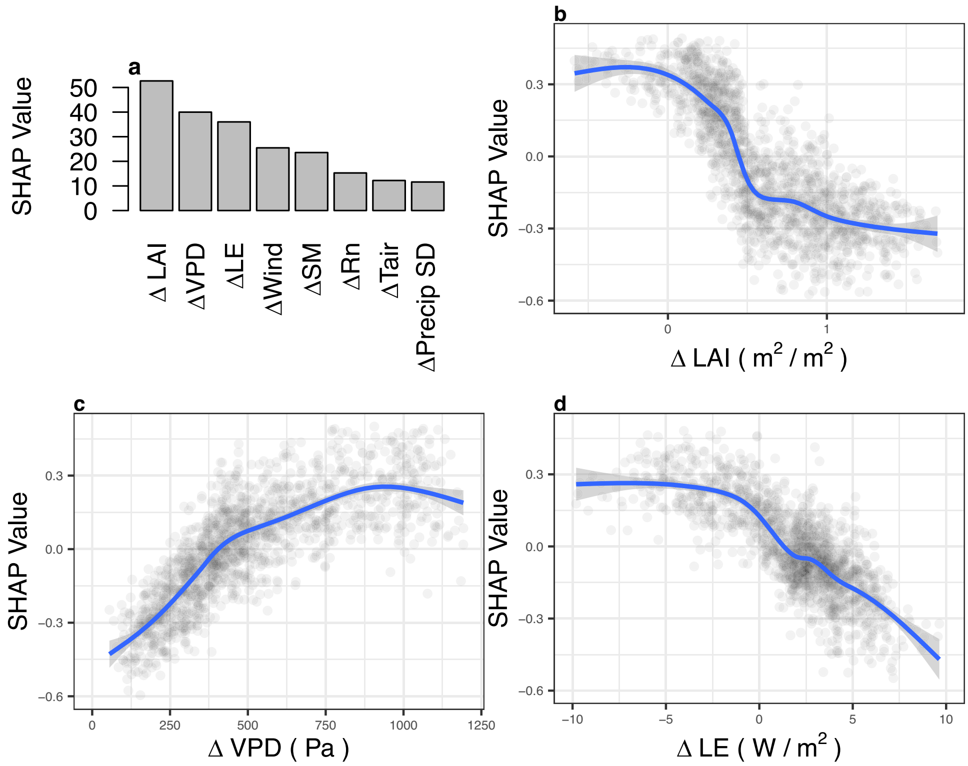

Fig. 2 | Shapley values for future changes in the difference between land surface and near-surface air temperature (ΔT) relative to the current day. a Shapley values converted to percentage of variance explained for all predictors explaining the pruned geographic distribution of the difference between the future ΔT (ΔT_{con_SSP585}) and current day ΔT (ΔT_{obs}). Shapley Values converted to percentage of variance explained for the top 3 predictors which are (**b**) changes between the historical and future simulations for mean leaf area index (LAI), (**c**) vapor pressure deficit (VPD), and (**d**) latent heat flux (LE). Other predictors used were changes in wind, soil moisture (SM), net radiation (Rn), air temperature (Tair) and the standard deviation of precipitation (Precip SD).

improve understanding of the rate at which this process can occur, and whether the maximum photosynthesis rate could be maintained[29]. While thermal acclimation has been observed, there is debate on whether broadleaf evergreen forests have the capability to acclimate as they tend to exist in historically stable environments with relatively small meteorological fluctuations[30,31]. Nevertheless, processes related to ecosystem acclimation are generally not incorporated in ESMs, and thus warrant more attention to improve ESM projections.

Although most vegetated regions exhibit increases in constrained ΔT in the future, there are several exceptions. Decreases are predicted in the Sahel and eastern Africa, parts of China, and certain regions in the Northern Latitudes including Alaska, Eastern Russia and northern Norway. These regions are predicted to have increases in future soil moisture, and less extreme increases in VPD compared to the Central US and Europe (Supplementary Fig. 8), implying that vegetation water stress will likely be less prevalent there than in other regions, and may even reduce. Many of these regions are also projected to have large future increases in LAI with increasing temperatures, which would lead to greater latent heat flux from increased transpiration.

Earth system model biases

When examined regionally, the ESM ensemble median ΔT bias in the historical simulation compared to ΔT_{obs} is varied, underestimating ΔT in 54% of vegetated areas (Fig. 3a), including regions of the tropics, and areas of overestimation present in Canada and Eastern Europe. In the future, the bias underestimation compared to ΔT_{con_SSP585} expands to 60% of vegetated areas, albeit with regional variations (Fig. 3b). However, when the difference between the future ΔT change and the current day is examined, the underestimation by the ESM median ensemble grows to 66% of vegetated areas (Fig. 3c). These biases are found across latitudes, with some exceptions in areas bordering dryer less vegetated regions (our study region edges), and parts of the northern latitudes including Central Canada and Eastern Russia. There are also large differences between individual ESMs.

Because of the strong influence of ΔT on carbon, water and energy fluxes, it is essential to correct these ESM biases to reduce uncertainty in future climate projections. Underestimation of the change in ΔT between the future and current-day in ESMs implies that more energy will be dissipated in ESMs as latent rather than sensible heat flux, particularly in a warmer future, which could bias the surface energy balance.

Discussion

The large, predicted rise in constrained ΔT over most vegetated regions compared to the current day indicates that using Tair to study ecosystem response to temperature increases would lead to large underestimation of real heat impacts on vegetation carbon uptake. It calls into question the use of Tair rather than LST to define Topt. From a physiological standpoint, it is elevated LST rather than Tair that drives reductions in photosynthesis from its impact on the maximum carboxylation and electron transport rates, while higher LST also drives increased respiration from temperature impacts on plant metabolic rates[32]. Meanwhile, because of coupling between the carbon and water cycles through stomata, and the temperature and VPD relationship through the Clausius-Clapeyron relation, using Tair rather than LST to study water cycle responses to VPD would also lead to misrepresentation of changes in latent heat flux, because transpiration increases in response to rising leaf surface VPD (which can vary from VPD of the air) until moisture limitation and stomatal closure, at which point it would decline[33]. Once stomatal conductance is sufficiently reduced, this can result in a feedback loop, where the impact of rising LST on vegetation through its direct and indirect effects (e.g., elevated

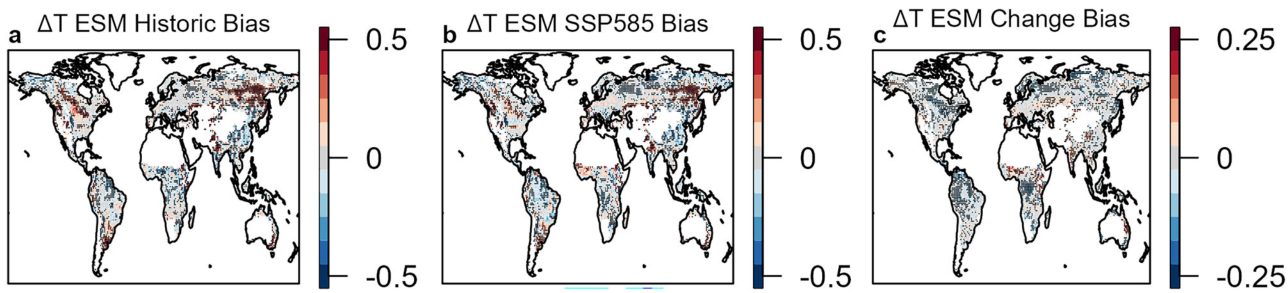

Fig. 3 | Earth System Model (ESM) biases in the difference between land surface temperature (LST) and air temperature (Tair) (ΔT). a The historic ESM bias calculated as the difference between the median ΔT across the ESM ensemble over 2000-2014 (ΔT_{ESM_Hist}) and the current day ΔT (ΔT_{obs}). **b** The future SSP585 ESM bias calculated as the difference between the median ΔT across the ESM ensemble for 2085–2099 (ΔT_{ESM_SSP585}) and the constrained future estimate (ΔT_{con_SSP585}). **c** The ESM bias for the change between the future and historic simulations calculated as the difference between ΔT_{ESM_SSP585} minus ΔT_{ESM_Hist} and ΔT_{con_SSP585} minus ΔT_{obs}. Blue areas represent where the median ESM ensemble underestimates ΔT, while red regions represent where it is overestimated. Hatched areas represent where at least 60% of the ESMs agree on the sign of the bias depicted.

VPD) can further drive ΔT increases, because reductions in transpiration and LAI from vegetation stress subsequently lead to more net radiation being partitioned into sensible rather than latent heat flux. This further warms the leaves, as transpiration serves as a cooling mechanism, and reduces vegetation carbon uptake, leaving more CO_2 in the atmosphere further contributing to rising temperatures.

It is also conceivable that our constrained future ΔT increases are underestimated, as ESMs do not represent certain processes that would further contribute to elevated ΔT. For example, ESMs do not include representation of leaf thermal damage, leaf shedding (to reduce water needs)[18,19], or mortality events in response to extreme temperatures. Also omitted from ESMs is the interaction between vegetation stress and disturbances such as fire[34] or insect/pathogen outbreaks[35]; stressed vegetation is oftentimes more vulnerable to these disturbances. Additionally, while vegetation can acclimate to warming temperatures[30], this process is not typically included in ESMs. These ESM omissions are clear sources of systematic uncertainty in the constrained future ΔT.

Likewise, we emphasize that the constrained regional ΔT increases of 0.25–0.5 °C by 2100 are conservative estimates of what ΔT has the potential to reach, because the data used in this study are monthly averages taken at regional scale (1.25 × 0.9375 degrees). One pixel samples a wide range of leaf conditions, some shaded, and some sunlit, indicating that some ΔT values are much greater than what these results reflect from spatial averaging[36]. Similarly, averaging ΔT at a monthly timescale conceals high daily ΔT values that occur during extreme events, such as droughts, which are predicted to increase in intensity and frequency in the future[37]. During a drought or heatwave, daily ΔT can increase because reduced water availability and increased atmospheric demand leads to lower canopy conductance and eventually transpiration[33]. These transpiration reductions, accompanied by lower soil evaporation, reduce latent heat flux and increase sensible heat flux, increasing ΔT, and driving leaf surface VPD increases. This can create a feedback loop that can prolong and exacerbate drought conditions[18], placing more stress on vegetation. Meanwhile, a drought can easily become a compound event accompanied by excessive heat, from LST increases driving sensible heat flux from the increased energy absorbed by vegetation, leading to further increases in Tair through land-atmosphere feedbacks[38–40]. During these types of events, even with LST driving increases in Tair, we would expect ΔT to be larger than what is depicted here, from this modification of the surface energy balance from vegetation stress. Likewise, hourly values of ΔT can also be higher than what is reflected here around solar noon. In fact, most of the ΔT increases present in the ESMs are driven by increases during midday and early afternoon (Supplementary Fig. 14). This implies that many more leaves could be operating above Topt at particular times of day, while leaf thermal damage can occur within minutes[32].

Since increasing VPD is a top driver of increases in future constrained ΔT (Fig. 2) regardless of aridity and plant functional type (Supplementary Figs. 10 and 12), and increased atmospheric CO_2 increases VPD[24], reducing CO_2 emissions could limit these moisture changes and attenuate future ΔT increases. To test this, we examined the changes in constrained ΔT using shared socio-economic pathway with an added radiative forcing of 4.5 W/m^2 by 2100 (SSP245). We found that the ΔT increases by 2100 are largely reduced compared to SSP585 (ΔT increases from 0.70 °C in the historical simulation to 0.75 °C in SSP245 rather than 0.81 °C in SSP585) (Supplementary Fig. 12). This demonstrates that increasing CO_2 impacts ΔT. To further investigate the CO_2 effect on ΔT we examined ESM projections of ΔT using 1 percent CO_2 simulations (Methods), where atmospheric CO_2 is increased by 1 percent in the atmosphere each year[41]. Our results showed that ΔT tended to be lower when the impacts of CO_2 fertilization on biogeochemistry were considered[42], versus when simply the radiative effects were included (Supplementary Fig. 16). While this may seem counterintuitive as increased atmospheric CO_2 has been shown to drive reduced stomatal conductance (and lower transpiration)[43,44] and can locally increase LST[45], it has also been demonstrated that this effect can be offset by increases in LAI from the effect of CO_2 fertilization in stimulating plant growth[44]. This implies that preventing LAI reductions through limiting deforestation and forest degradation could be part of a solution to keep temperature increases to a minimum even with increasing CO_2[42,46]. It demonstrates that reduced stomatal closure in response to higher atmospheric CO_2[47] is not leading to less evaporative cooling, likely from increased LAI[42].

Lastly, although our results represent average constrained values and cannot explicitly capture extremes or diurnal variability, they do not support the limited homeothermy theory—which posits that plants regulate leaf temperature toward Topt, resulting in LST exceeding Tair when Topt is higher and falling below Tair when Topt is lower. On average, our findings show that LST remains consistently greater than Tair. Adding to this, we also demonstrate that LST is increasing at a greater pace than Tair under rising atmospheric CO_2, suggesting that canopy temperatures accelerate toward Topt more rapidly compared to the warming of ambient air. While this does not necessarily imply that there is no thermoregulation, as it simply suggests that leaves are not able to cool more than the air, with many studies demonstrating that ecosystems are already operating near their Topt[23], this demonstrates that vegetation may not be capable of maintaining leaf temperatures that maximize photosynthesis as heat levels rise, and rates of respiration may increase[29], with negative implications for carbon uptake and the atmospheric CO_2 growth rate.

The difference between land surface (LST) and near-surface air temperature (Tair) provides a key indicator of the physical and biological processes governing ecosystem function and structure. Our results show that this temperature difference (ΔT) is increasing in most regions of the world, with significant implications for global carbon, water and energy fluxes, and that ESMs largely misrepresent these changes. Rising ΔT indicates that vegetation is likely to experience greater thermal and hydraulic stress in the future, leading to reduced net carbon uptake, transpiration and latent heat flux. Regions particularly at risk include the margins of tropical rainforests, Central US expanding into Canada, and Southern Europe. The underestimation of ΔT in ESMs suggests that these models could overestimate future net carbon uptake and misrepresent the surface energy balance. To reduce this bias, we need an improved understanding of the interactions between vegetation, ΔT, and the climate system, which requires better estimates of LST. We emphasize that studies investigating temperature and VPD effects on vegetation dynamics should rely on LST rather than Tair, as LST is more directly related to ecosystem function. Doing so will reduce systematic underestimation of temperature and VPD effects on vegetation. Improved observational products and analytical approaches to capture the interactions between vegetation, ΔT, and climate will improve our ability to represent land-atmosphere feedbacks in ESMs. Ultimately, this will reduce uncertainty in future climate projections and enhance our understanding of ecosystem responses to environmental change.

Methods

Emergent constraints

An emergent constraint requires the presence of a strong physical and statistical relationship between an observable (X) and an unobservable variable (Y) that is represented in an ensemble of models[15,16]. While individual models may have incorrect values for variables X and Y, if the heuristic relationships between them are preserved across the model ensemble, when examined together, the consistency of this relationship allows for the use of observational data of X to constrain the unobservable (modeled) variable Y. For an effective constraint, the relation between X and Y needs to be based on underlying physical principles.

Here, we first apply an emergent constraint using observational Tair ('tas') data to constrain the all-sky LST ('ts') in the historic simulation of CMIP6 across ESMs for the 2000–2014 time period (Supplementary Table 1). While observations of LST are available, thermal satellite products only represent clear-sky conditions and have large differences between datasets (Supplementary Fig. 1), while microwave all-sky LST data has high uncertainty associated with it[8]. Thus, we can instead use the emergent constraint approach, because LST and Tair are highly correlated across space and time, and influence each other through land-atmosphere feedbacks. For the observational Tair, we used four datasets for the 2000–2020 period at a monthly temporal resolution that consisted of reanalysis and ground-based derived products. These datasets include the 5th generation of the European Center for Medium-Range Weather Forecasts atmospheric reanalysis of the global climate (ERA5[48]), the Global Historical Climatology Network and the Climate Anomaly Monitoring System (GHCN-CAMS[49]), the Climate Research Unit (CRU[50]), and the Berkeley Earth Surfaces Temperature (BEST[51]) dataset (Supplementary Fig. 1). For the analysis, we were interested in understanding changes in ΔT and its feedbacks with vegetation, and thus we focused on growing season data, which we defined as those months when the local monthly temperature climatology was greater than 5 °C, and the monthly net radiation climatology was at least 60% of the local maximum monthly climatological value. This filter was applied for each ESM individually based on the 'tas' and net radiation data (the sum of the short-wave and long-wave radiation: 'rsds'+'rlds'-'rsus'-'rlus') of each ESM from 1950-2014. For the observation-based datasets, Tair data was used from ERA5 and net radiation was used from the Clouds and the Earth's Radiant Energy System (CERES)[52] to filter the observational Tair[48,52] from the years 2000–2020. We also constrained the analysis to regions and months where the average climatology of LAI was greater than 1, filtering each ESM dataset using their own '*lai*' output, and filtering the observational data based on the observation-based Global Monthly Mean Leaf Area Index Climatology from 1981–2015[53]. We also repeated these analyses using an LAI filter of 2, to ensure that the results were not being misrepresented due to soil contamination, and achieved similar results, although we were able to constrain fewer pixels (Supplementary Fig. 17). All ESM and observational monthly data were bilinearly interpolated to a common resolution of the finest scale ESM, which was a 288 by 192 grid scheme. Because of the tight relationship between the LST and Tair data across the ESMs (Supplementary Fig. 2a), we were able to apply the constraint on LST pixel-by-pixel to create an all-sky LST global average of the current day. This was repeated for all 4 observation-based Tair datasets resulting in 4 constrained maps of current day all-sky LST (Supplementary Fig. 2a, c, e, g).

For the second emergent constraint, we used the difference between the observation-based constrained LST and observation-based Tair (using the Tair data from ERA5, GHCN CRU, and BEST) to constrain future growing season ΔT (2085-2099) in the high emission pathway with an added radiative forcing of 8.5 W/m^2 (SSP585) by 2100 across CMIP6 ESMs. Due to the tight relationship between the present and future ΔT data across the ESMs (Fig. 1a, Supplementary Fig. 3b) we were able to apply the constraint pixel-by-pixel (R^2, the fraction of variance explained by the model > 0.6 in 96% of pixels) to achieve a regional understanding of how ΔT will change in the future in this business-as-usual scenario. We generated 4 constrained maps of ΔT based on the 4 different Tair observational and constrained LST products, which had similar spatial patterns and values to each other (Supplementary Fig. 2b, d, f, h). In Fig. 1, the median value across the 4 observation-based products is shown. This analysis was also repeated using the low/medium emission pathway with an added radiative forcing of 4.5 W/m^2 (SSP245) by 2100 across CMIP6 ESMs (Supplementary Fig. 15) to deduce how the effects of less extreme anthropogenic emissions might impact future ΔT.

For each emergent constraint, we quantified the uncertainty in our independent variable using the per-pixel standard deviation across the 4 observation-based datasets averaged, and in our ESM ensemble linear regression using the standard error. We then propagated these uncertainties to quantify an uncertainty of our emergent constraint (Fig. 1 and Supplementary Fig. 15). It should be noted that the implicit assumption of an emergent constraint is that there are no strong systematic biases/omitted processes across the model ensemble used for the constraint related to the variables of interest.

To understand how future ΔT changes might vary across aridity gradients, we binned the data based on the aridity index (AI) (Supplementary Fig. 4), the ratio of potential evapotranspiration to precipitation, and re-plotted the emergent constraint per bin using the same temperature datasets as the global analysis (Supplementary Fig. 5). Regions were characterized as arid ($AI < 0.5$), subhumid ($0.5 < AI < 0.65$) or humid ($AI > 0.65$), and the aridity index was calculated using monthly data from CRU. We also investigated the impact of plant functional type on future ΔT changes by binning the data by MODIS PFTs from 2015, before re-plotting the emergent constraint per PFT (Supplementary Figs. 4 and 7). Because the MODIS PFT data is retrieved at a 0.05-degree spatial resolution, the data had to be interpolated to the coarser spatial resolution of the ESMs before analysis. Pixels were only used if at least 75% of the finer resolution pixels agreed on the PFT (Supplementary Fig. 4).

Aridity and future moisture changes

To gain an understanding of the interactions between aridity and drying and wetting trends on the projected ΔT changes, we binned the data based on the aridity index (AI), the ratio of potential evapotranspiration to precipitation calculated using data from CRU, as well as drying and wetting trends based on the mean ESM ensemble of future changes in precipitation ('pr') and surface soil moisture ('mrsos'). Regions were characterized as arid (AI < 0.5), subhumid (0.5 < AI < 0.65) or humid (AI > 0.65). They were further grouped as drying (future projected precipitation or soil moisture is lower than that of today) or wetting (future projected precipitation or soil moisture is greater than that of today). These bins were used to create the violin plots displayed in Supplementary Fig. 6.

Random forest models and shapley values

We applied a random forest model (RF)[54] using the R package 'ranger'[55] to explore whether there were certain environmental and climatological traits that were predicted to change between the future and current day that could be used to characterize how constrained ΔT changed between the future and current time periods. As predictors, we used variables that were calculated from the mean CMIP6 ESM ensemble as the change between the future (2085–2100) and near-current (2000–2014) time periods that described mean and median changes in meteorological conditions and vegetation structure. We used the change in mean growing season LAI, latent heat flux, VPD, soil moisture, net radiation, Tair, surface wind speed, and the standard deviation of precipitation. We did not include predictor variables that had correlations with each other or the response variables of greater than 0.7 to avoid issues of misattribution, which led to the exclusion of the average sensible heat flux change (highly correlated with temperature), and several other metrics related to temperature and moisture variability. The correlation between predicted changes in SM and VPD was below 0.7, but since SM and VPD are frequently highly correlated at the monthly timescale[24], to ensure that the inclusion of both predictor variables did not lead to misattribution, we re-ran the RF with changes in VPD removed and confirmed that this did not lead to changes in SM becoming a more important predictor. Annual precipitation was not included due to its strong relationship with net radiation and soil moisture. We did not include predictor variables that described current environmental conditions (e.g., AI, land cover type, and topography from observational sources) because we determined that they contributed limited predictive information using recursive feature elimination.

Since we were using spatial data for the RF model, spatial autocorrelation within the data was a concern. We calculated Global Moran's I values using the R package 'ncf'[56] with a spline (cross-) correlogram function (Supplementary Fig. 9), and discovered that the data was indeed spatially autocorrelated using the 1.25 degree longitude by 1.067 degree latitude spatial resolution of the data, which near the equator is equivalent to approximately 138.75 km east-west by 118 km north-south. However, the spatial autocorrelation greatly declined when using pixels further apart. We therefore ran the RF model on every other pixel (Supplementary Fig. 9) for regions between 57°S and 57°N, so that pixel centroids were approximately 277.5 km apart east-west and 236 km apart north-south near the equator, removing artefacts of spatial autocorrelation. The distances between pixel centroids declines in the east-west direction as we moved towards the poles, and therefore above 57°N we only used one in every 4 pixels east-west. Using this approach, we were able to ensure that our RF model and Shapley value results were not impacted by spatial autocorrelation (Fig. 2 and Supplementary Fig. 9).

For each RF, the number of trees used (capped at a maximum of 500) and the number of variables to split at each node (between 2 and the total number of predictor variables) were optimized to produce the lowest out-of-bag error (based on approximately one third of the observations[54]). Each RF was trained to predict the values of ΔT changes between the constrained future and historical simulations. The R^2 value on out-of-bag data was 0.75 on the optimized model.

Shapley values were generated for each RF model using the R package 'fastshap'[57] to determine the most influential predictors for explaining the ΔT changes between the present and future time periods (Fig. 2). These values were converted to the percentage of variability explained by each predictor, by dividing the Shapley values of each variable by the sum of the absolute values of the Shapley values of all predictors. While Shapley values are an effective way to visualize predictor-response interactions in machine learning algorithms, it should be noted that these relationships are not necessarily indicative of causality. Nevertheless, the exclusion of correlated predictor variables from the RF models leaves us confident that the variable relationships depicted by the Shapley values reveal important relationships between environmental variables influencing changes in future ΔT.

To understand how drivers of future ΔT changes might vary across different environments, we binned the data based on the AI (arid, subhumid and humid) (Supplementary Fig. 4) and trained one new RF model per bin (out-of-bag R^2 of 76%, 73% and 84% accordingly). We again generated Shapley values for each bin to understand the most influential predictor variables and the nature of their interactions across aridity gradients. We repeated this process by binning the data by PFT (out-of-bag R^2 of 76%, 69%, 70%, 75%, 75%, 75% and 77% for evergreen broadleaf, mixed forest, open shrublands, woody savannas, savannas, grasslands, and croplands accordingly). We only generated models for PFTs that had at least 80 pixels, as it is standard practice to have at least ten times as much data as predictors (we used 8 predictors) for robust RF results. For these analyses, we did not prune the data for spatial autocorrelation, because this would have led to too few data points being available to run the RF models. However, the results were largely consistent with the globally pruned results.

3-hour ΔT Changes

To determine whether there was a particular time of day that was predominantly contributing to the increasing ΔT trend in ESMs, we compared 3-hourly data from the SSP585 scenario for the start (2015–2017) and end (2096–2098) of the simulations for those ESMs that included output at that temporal resolution (Supplementary Table 1). We applied the same LAI filters that were used for processing the monthly data and filtered the data to growing season months using only those months when the LAI climatology was greater than 1. We then calculated an average diurnal cycle of ΔT averaged across those remaining regions and computed the difference between the average cycle in 2015–2017 and 2097–2099. For each timestep, we created boxplots across the participating ESMs to determine that the increasing ΔT trend was mainly stemming from daytime rather than nighttime increases (Supplementary Fig. 14). For the MIROC-ES2L, we were unable to get data for the full time period, and thus those reflect only the difference between the single years of 2098 and 2015.

1 Percent CO_2 runs

To understand the influence of rising CO_2 on the ΔT changes in the future and its interactions with vegetation, we analyzed CMIP6 ESMs that had LST ('ts') and Tair ('tas') data available for the idealized Coupled Climate-Carbon Cycle Model Intercomparison Project[41] (Supplementary Table 1). This project is composed of a control run and two experiments. In the control simulation (1pctCO2), atmospheric CO_2 is increased by 1 percent per year from pre-industrial levels (285ppm). In the first experiment, the biogeochemically coupled experiment (1pctCO2-bgc), atmospheric CO_2 is increased by 1 percent per year from pre-industrial levels for carbon cycle elements in the ESM, but the radiation model of the ESM continues to see pre-industrial atmospheric CO_2 levels. In the second experiment, the radiatively coupled experiment (1pctCO2-rad), the radiation model of the ESM experiences the 1 percent per year rise in atmospheric CO_2 from pre-industrial times, but the carbon cycle elements see only pre-industrial levels. In these idealized experiments there is no land-use change or other greenhouse gas emissions to allow one to exclusively understand the influence of carbon fertilization from CO_2 emission on the signal of ΔT in isolation from the impacts of other potential drivers. For each ESM we took the average ΔT value per year over all areas where our results showed a future increase in ΔT (Fig. 1), and then plotted the mean value across the ESMs for 1885-1925 (representing CO_2 concentrations ranging from ~404 ppm to ~601 ppm).

Data availability

The remote sensing, reanalysis, and ESM data used in this study are freely available from the following sources: • AIRS land surface temperature[14]: https://disc.gsfc.nasa.gov/datasets/AIRS3STM_7.0/summary?keywords • BEST near surface air temperature[51]: https://storage.googleapis.com/berkeley-earth-temperature-hr/global/gridded/Global_TAVG_Gridded_1deg.nc • CERES net radiation[52]: https://ceres-tool.larc.nasa.gov/ord-tool/jsp/EBAF421Selection.jsp • CMIP6 historical/future/1%CO_2 simulations[17]: https://esgf-node.llnl.gov/search/cmip6/ • CRU precipitation, near surface air temperature, and potential evaporation[50]: https://catalogue.ceda.ac.uk/uuid/c26a65020a5e4b80b20018f148556681 • ERA5 near surface air temperature[48]: https://cds.climate.copernicus.eu/cdsapp#!/dataset/reanalysis-era5-single-levels-monthly-means?tab=overview • ERA5 skin temperature[48]: https://cds.climate.copernicus.eu/datasets/reanalysis-era5-single-levels?tab=download • GHCN CAMS near surface air temperature[49]: https://psl.noaa.gov/data/gridded/data.ghcncams.html • Global mean leaf area index climatology, 1981–2015[53]: https://daac.ornl.gov/cgi-bin/dsviewer.pl?ds_id=1653 JULY 8 2022 • MODIS 11 land surface temperature[12]: https://lpdaac.usgs.gov/products/mod11c3v061/ • MODIS 21 land surface temperature[13]: https://lpdaac.usgs.gov/products/myd21v061/ • MODIS 12 land cover type[58]: https://www.earthdata.nasa.gov/data/catalog/lpcloud-mcd12c1-061. The processed ESM data, constrained maps, RF model output and Shapley values generated in this study have been deposited in the Code Ocean database under accession code https://doi.org/10.24433/CO.1603955.v1.

Code availability

The code and data used to perform main figure analyses and generate figures are available on Code Ocean, https://doi.org/10.24433/CO.1603955.v1.

References

1. United Nations Framework Convention on Climate Change (UNFCCC). Paris Agreement to the United Nations Framework Convention on Climate Change T.I.A.S. No. 16-1104 (2015).
2. Still, C. et al. Thermal imaging in plant and ecosystem ecology: applications and challenges. *Ecosphere* **10**, e02768 (2019).
3. De Boeck, H. J., Van De Velde, H., De Groote, T. & Nijs, I. Ideas and perspectives: heat stress: more than hot air. *Biogeosciences* **13**, 5821–5825 (2016).
4. Good, E. J. An in situ-based analysis of the relationship between land surface "skin" and screen-level air temperatures. *J. Geophys. Res.* **121**, 8801–8819 (2016).
5. Green, J. K. et al. Surface temperatures reveal the patterns of vegetation water stress and their environmental drivers across the tropical Americas. *Global Change Biol.* 1–16 https://doi.org/10.1111/gcb.16139 (2022).
6. Cai, D. et al. Using sub-diurnal surface-air temperature difference anomaly derived from Himawari-8 geostationary satellite and meteorological grids for early detection of vegetation drought stress: application to Australia's 2017–2019 Tinderbox Drought. *Remote Sens. Environ.* **327**, 114768 (2025).
7. Good, E. J., Aldred, F. M., Ghent, D. J., Veal, K. L. & Jimenez, C. An analysis of the stability and trends in the LST_cci land surface temperature datasets over Europe. *Earth Space Sci.* **9**, e2022EA002317 (2022).
8. Kan, F. et al. Discrepant trends in global land-surface and air temperatures controlled by vegetation biophysical feedbacks. *Environ. Res. Lett.* **18**, 124013 (2023).
9. Li, Z. et al. Satellite remote sensing of global land surface temperature: definition, methods, products, and applications. *Rev. Geophys.* **61**, e2022RG000777 (2023).
10. Song, P., Zhao, T., Zhang, Y. & He, Q. Conversion of satellite passive microwave signals to land surface "skin" temperature for extremely dry deserts. *Remote Sens. Environ.* **299**, 113857 (2023).
11. Gallo, K. & Krishnan, P. Evaluation of the bias in the use of clear-sky compared with all-sky observations of monthly and annual daytime land surface temperature. *J. Appl. Meteorol. Climatol.* **61**, 1485–1495 (2022).
12. Wan, Z. Collection-6.1 MODIS Land Surface Temperature Products Users' Guide. https://doi.org/10.5067/MODIS/MOD11C3.061 (2019).
13. Hulley, G., Freepartner, R., Malakar, N. & Sarkar, S. *Moderate Resolution Imaging Spectroradiometer (MODIS) Land Surface Temperature and Emissivity Product (MxD21) User Guide*. 37 (2019).
14. AIRS Project. Aqua/AIRS L3 Monthly Standard Physical Retrieval (AIRS-only) 1 degree x 1 degree V7.0. Goddard Earth Sciences Data and Information Services Center (GES DISC) https://doi.org/10.5067/UBENJB9D3T2H (2019).
15. Hall, A., Cox, P., Huntingford, C. & Klein, S. Progressing emergent constraints on future climate change. *Nat. Clim. Change* **9**, 269–278 (2019).
16. Williamson, M. S. et al. Emergent constraints on climate sensitivities. *Rev. Mod. Phys.* **93**, 1–39 (2021).
17. Eyring, V. et al. Overview of the Coupled Model Intercomparison Project Phase 6 (CMIP6) experimental design and organization. *Geosci. Model Dev.* **9**, 1937–1958 (2016).
18. Schumacher, D. L., Keune, J., Dirmeyer, P. & Miralles, D. G. Drought self-propagation in drylands due to land–atmosphere feedbacks. *Nat. Geosci.* **15**, 262–268 (2022).
19. Koppa, A. et al. Dryland self-expansion enabled by land–atmosphere feedbacks. *Science* **385**, 967–972 (2024).
20. Gentine, P. et al. Land-atmosphere interactions in the tropics—a review. *Hydrol. Earth Syst. Sci.* **23**, 4171–4197 (2019).
21. Chen, C. et al. Biophysical effects of croplands on land surface temperature. *Nat. Commun.* **15**, 10901 (2024).
22. Flores, B. M. et al. Critical transitions in the Amazon forest system. *Nature* **626**, 555–564 (2024).
23. Doughty, C. E. et al. Tropical forests are approaching critical temperature thresholds. *Nature* **621**, 105–111 (2023).
24. Green, J. K. The intricacies of vegetation responses to changing moisture conditions. *N. Phytol.* **244**, 2156–2162 (2024).
25. Piao, S. et al. Characteristics, drivers and feedbacks of global greening. *Nat. Rev. Earth Environ.* **1**, 14–27 (2019).
26. Duveiller, G., Hooker, J. & Cescatti, A. The mark of vegetation change on Earth's surface energy balance. *Nat. Commun.* **9**, 679 (2018).
27. Wuyts, B., Champneys, A. R. & House, J. I. Amazonian forest-savanna bistability and human impact. *Nat. Commun.* **8**, 15519 (2017).
28. Fang, Z. et al. Global increase in the optimal temperature for the productivity of terrestrial ecosystems. *Commun. Earth Environ.* **5**, 466 (2024).
29. Slot, M. & Winter, K. In situ temperature response of photosynthesis of 42 tree and liana species in the canopy of two Panamanian lowland tropical forests with contrasting rainfall regimes. *N. Phytol.* **214**, 1103–1117 (2017).
30. Liu, J. et al. Evidence for widespread thermal acclimation of canopy photosynthesis. *Nat. Plants* https://doi.org/10.1038/s41477-024-01846-1 (2024).
31. Huang, M. et al. Air temperature optima of vegetation productivity across global biomes. *Nat. Ecol. Evol.* **3**, 772–779 (2019).
32. Wahid, A., Gelani, S., Ashraf, M. & Foolad, M. Heat tolerance in plants: an overview. *Environ. Exp. Bot.* **61**, 199–223 (2007).
33. Grossiord, C. et al. Plant responses to rising vapor pressure deficit. *N. Phytol.* **226**, 1550–1566 (2020).

34. Ray, D., Nepstad, D. & Moutinho, P. Micrometeorological and canopy controls of fire susceptibility in a forested Amazon landscape. *Ecol. Appl.* **15**, 1664–1678 (2005).
35. Choat, B. et al. Triggers of tree mortality under drought Drought and forest mortality. *Nature* **558**, 531–539 (2018).
36. Manzi, O. J. L. et al. Canopy temperatures strongly overestimate leaf thermal safety margins of tropical trees. *New Phytol.* nph.20013 https://doi.org/10.1111/nph.20013 (2024).
37. Lee, H. et al. *Climate Change 2023: Synthesis Report: Summary for Policymakers*. https://www.ipcc.ch/report/ar6/syr/ 10.59327/IPCC/AR6-9789291691647 (2023).
38. García-García, A. et al. Soil heat extremes can outpace air temperature extremes. *Nat. Clim. Chang.* https://doi.org/10.1038/s41558-023-01812-3 (2023).
39. Li, J. et al. Future increase in compound soil drought-heat extremes exacerbated by vegetation greening. *Nat. Commun.* **15**, 10875 (2024).
40. Zhou, S. et al. Land–atmosphere feedbacks exacerbate concurrent soil drought and atmospheric aridity. *Proc. Natl. Acad. Sci. USA* **116**, 18848–18853 (2019).
41. Jones, C. D. et al. C4MIP-the coupled climate-carbon cycle model intercomparison project: experimental protocol for CMIP6. *Geosci. Model Dev.* **9**, 2853–2880 (2016).
42. Zeng, Z. et al. Climate mitigation from vegetation biophysical feedbacks during the past three decades. *Nat. Clim. Change* **7**, 432–436 (2017).
43. Betts, R. A. et al. Projected increase in continental runoff due to plant responses to increasing carbon dioxide. *Nature* **448**, 1037–1041 (2007).
44. Betts, R. A., Cox, P. M. & Woodward, F. I. Simulated responses of potential vegetation to doubled-CO2 climate change and feedbacks on near-surface temperature. *Glob. Ecol. Biogeogr.* **9**, 171–180 (2000).
45. Long, S. P., Ainsworth, E. A., Leakey, A. D. B., Nösberger, J. & Ort, D. R. Food for thought: lower-than-expected crop yield stimulation with rising CO_2 concentrations. *Science* **312**, 1918–1921 (2006).
46. Rangel Pinagé, E. et al. Surface energy dynamics and canopy structural properties in intact and disturbed forests in the Southern Amazon. *JGR Biogeosci.* **128**, e2023JG007465 (2023).
47. Ruehr, S. et al. Evidence and attribution of the enhanced land carbon sink. *Nat. Rev. Earth Environ.* **4**, 518–534 (2023).
48. Hersbach, H. et al. ERA5 monthly averaged data on single levels from 1940 to present. Copernicus Climate Change Service (C3S) Climate Data Store (CDS). https://doi.org/10.24381/cds.f17050d7 (2023).
49. Fan, Y. & Van Den Dool, H. A global monthly land surface air temperature analysis for 1948–present. *J. Geophys. Res.* **113**, 2007JD008470 (2008).
50. Harris, I., Osborn, T. J., Jones, P. & Lister, D. avid Version 4 of the CRU TS monthly high-resolution gridded multivariate climate dataset. *Sci. Data* **7**, 1–18 (2020).
51. Rohde, R. A. & Hausfather, Z. The Berkeley Earth Land/Ocean Temperature Record. *Earth Syst. Sci. Data* **12**, 3469–3479 (2020).
52. Wielicki, B. A. et al. Clouds and the Earth's Radiant Energy System (CERES): an earth observing system experiment. *Bull. Am. Meteor. Soc.* **77**, 853–868 (1996).
53. Mao, J. & Yan, B. Global Monthly Mean Leaf Area Index Climatology, 1981–2015. ORNL DAAC, Oak Ridge, Tennessee, USA. https://doi.org/10.3334/ORNLDAAC/1653 (2019).
54. Breiman, L. Random forests. *Mach. Learn.* **45**, 5–32 (2001).
55. Wright, M. N. & Ziegler, A. Ranger: a fast implementation of random forests for high dimensional data in C++ and R. *J. Stat. Softw.* **77**, 1–17 (2017).
56. Bjornstad, O. N. ncf: Spatial Covariance Functions. R package version 1.3-2 (2022).
57. Greenwell, B. *Fastshap: Fast Approximate Shapley Values* https://cran.r-project.org/package=fastshap (2020).
58. Friedl, M. & Sulla-Menashe, D. MODIS/Terra+Aqua land cover type yearly L3 global 0.05Deg CMG V061. *NASA Land Processes Distributed Active Archive Center* https://doi.org/10.5067/MODIS/MCD12C1.061 (2022).

Acknowledgements

We acknowledge the World Climate Research Program, which, through its Working Group on Coupled Modeling, coordinated and promoted CMIP6. We thank the climate modeling groups for producing and making available their model output, the Earth System Grid Federation (ESGF) for archiving the data and providing access, and the multiple funding agencies who support CMIP6 and ESGF. T.F.K. acknowledges support from a NASA awards 80NSSC21K1705 and 80NSSC25K7327, the RUBISCO SFA, which is sponsored by the Regional and Global Model Analysis (RGMA) Program in the Climate and Environmental Sciences Division (CESD) of the Office of Biological and Environmental Research (BER) in the U.S. Department of Energy (DOE) Office of Science, and additional support from a DOE Early Career Research Program award #DE-SC0021023.

Author contributions

J.K.G. designed the study with substantial input from T.F.K.; J.K.G. processed the data, ran the analyses and drafted the paper. X.L., P.C., D.J.P.M. and T.F.K. contributed to figure and data interpretation. All authors contributed comments and revisions to the manuscript.

Competing interests

The authors declare no competing interests.

Additional information

Supplementary information The online version contains supplementary material available at https://doi.org/10.1038/s41467-026-73063-7.

Correspondence and requests for materials should be addressed to Julia K. Green.

Peer review information *Nature Communications* thanks Yongjie Pan and Dominik Schumacher for their contribution to the peer review of this work. A peer review file is available.